A LANDSLIDE INVENTORY FOR PRINCE OF WALES ISLAND, ALASKA FROM 2009 TO 2023 USING PLANET IMAGERY

by

ELIZA LAWRENCE

A THESIS

Presented to the Department of Earth Sciences and Department of Geography
and the Robert D. Clark Honors College
in partial fulfillment of the requirements for the degree of
Bachelor of Science

November 2024

An Abstract of the Thesis of

Eliza Lawrence for the degree of Bachelor of Science in the Department of Earth Sciences and Department of Geography to be taken December 2024

Title: A Landslide Inventory for Prince of Wales Island, Alaska from 2009 to 2023 Using Planet Imagery

Approved: *Josh Roering, Ph.D.*
Primary Thesis Advisor

The combination of extreme rainfall brought on by atmospheric rivers and steep topography has made landslides a frequent and hazardous occurrence on Prince of Wales Island (PoW) in Southeast Alaska. Detecting and monitoring landslides on the ground can be costly and time-consuming, especially in remote and inaccessible locations. By using high-resolution (3-5 m) Earth observation imagery from Planet Labs, we can pinpoint the location and constrain the timing of past landslides through visual change detection of multiple images acquired every 2-3 days. We have mapped over 750 landslides across PoW (6670 km^2) and the surrounding islands from 2009 to 2023. By comparing pre- and post-landslide failure images, we determined landslide timing with temporal constraints ranging from one year to less than one week. This study expands upon the USFS Tongass National Forest Landslide Inventory, which utilizes a combination of decadal aerial photos and high-resolution satellite imagery, providing multi-year constraints on landslide timing. The inventory presented in this study includes landslide polygons, corresponding initiation points, and an attribute table containing the last pre-failure date, first post-failure date, slope, elevation, forest stand age, geology, distance to the nearest road, and area. The distribution of landslides across PoW over the past decade demonstrates a strong seasonality, with most landslides occurring between August and December. We find a

strong relationship between landslide location and aspect, with landslides predominantly occurring on southern slopes. Our methods also capture small landslides, revealing that most are located within 10 km of the nearest road. We find that cumulative precipitation, both monthly and annually, does not fully explain the relationship with landslide frequency and requires further exploration. Future research will use gridded precipitation data, coupled with well-characterized timing of landslides, to determine precipitation intensity thresholds for landslide triggering. By quantifying the temporal and spatial distribution of landslide occurrences, we can provide valuable information to support the development of landslide early-warning systems.

Acknowledgements

First, I would like to acknowledge that this project takes place on the ancestral homelands of the Tlingit and Haida peoples, whose histories and cultures are deeply intertwined with the coastlines, hillslopes, and forests of Southeast Alaska. I am grateful to the citizens of the Central Council of Tlingit and Haida Indian Tribes, who continue to serve as stewards of this land.

I am deeply indebted to Professor Josh Roering for his time, feedback, and unwavering support of this project over the past two years. His mentorship has been instrumental in my development as both a scientist and a student. I would also like to thank Professor Annette Patton for her dedication to this project and her invaluable guidance during our fieldwork in August 2023. I am grateful to Professors Casey Shoop and Susheel Adusumilli for their participation on my thesis committee and for their feedback.

This thesis would not have been possible without the exceptional coursework of Professor Sarah Cooley and Professor Johnny Ryan, whose teaching provided the foundation for the methods and analyses used in this project. I am also appreciative of Jacquie Foss at the U.S. Forest Service for her advice on relevant data sources, and to Wade Hulstine at Shaan Seet Inc. for his insights on the impacts of recent landslide events on Prince of Wales Island. The completion of this project would not have been possible without Lia Godino, who worked on the final year of landslide mapping during the summer of 2024. I am grateful to the other members of the Earth Surface Processes Lab for their camaraderie and support.

Finally, I would like to thank my parents, Bob and Elizabeth, and my sister, Michaela, for their emotional and financial support and for proofreading many emails along the way. This project was made possible through funding from the University of Oregon Center for Undergraduate Research and Engagement and the National Science Foundation Kutí project.

Table of Contents

List of Figures

List of Tables

Introduction

Understanding where and when landslides have occurred in the past allows us to better predict where they will happen in the future. Despite their frequent occurrence and associated negative impacts across the mountainous landscape of Southeast Alaska (SEAK), information about the location and timing of landslide occurrences is not systematically documented at a high resolution in the region. Documenting the location and timing of past landslides in SEAK provides insights into topographical factors—such as aspect, slope, and elevation—and spatial relationships, including proximity to roads, geology type, and forest age, that influence hillslope susceptibility to landslides (van Westen, 2008; Guzzetti, 2012).

Landslide hazards in SEAK

The most damaging and frequent type of landslides in SEAK are shallow landslides and debris flows (Swanston and Marion, 1991; Johnson et al., 2000). A shallow landslide is typically only a few meters deep, but has a high fluid content, which allows it to gain speed and material as it travels downhill. Some shallow landslides turn into debris flows and travel for longer distances with more material. Shallow landslides are often triggered by intense rainfall events that exceed soil drainage capability. Since debris flows have a high velocity, they often have long runouts and can have an unpredictable direction. Debris flows happen quickly, making it difficult to provide people with warning. Due to the velocity and the amount of earth that can be displaced by landslides, they pose serious risks to the safety of communities across the world, and particularly in SEAK.

Landslides in SEAK are persistent hazards to the small, remote communities that are situated at the base of steep hillslopes (Patton et al., 2022). In SEAK, past landslides have blocked roads and damaged homes and infrastructure. As they become more frequent and

harmful, the desire to better understand their location and timing has increased. In Kasaan, a small town on the eastern side of Prince of Wales Island (PoW), a landslide blocked the main road and cut the area off from outside vehicular transportation for multiple months. Landslides in SEAK have also been fatal. On December 2nd, 2020, a landslide in Haines, Alaska, destroyed three residences, severely damaged a fourth, and took the lives of two occupants (Darrow, 2022). In Wrangell, Alaska, a landslide on November 20th, 2023, killed six people and destroyed two homes (Nicolazzo, 2024). These events demonstrate the need to understand the past behavior and potential of landslides to better protect communities.

Landslide Inventories

Detecting and monitoring landslides can be costly and time-consuming, especially when they occur in remote and inaccessible locations. Since the launch of Landsat-1 in 1972, the earliest earth observation satellite, remote sensing techniques were recognized as a useful tool for studying landslides because they provide systematic and spatially extensive information about the land surface, without having to be on the ground, which can be dangerous and imprecise (Casagli, 2023).

Satellite imagery can be used to pinpoint the location and timing of past events because of the visual change that destructive landslides cause to hillslopes and vegetation. Visual analysis is particularly effective to map landslides in forested terrain, where the slope failures have left clear signs of the occurrence. Over the past 50 years, the quality of satellite imagery has continually increased, which has created a plethora of remotely sensed landslide inventories.

Landslide inventories using high-resolution imagery have been created in many areas of the world, especially after natural disasters such as earthquakes and large rainfall events (Piralilou, 2019; Roback, 2017; Shao 2019). Many inventories are event-based, meaning they

map all landslides in response to a known trigger with a known date. For example, a rainfall-induced inventory of the Lower Mekong River Valley, which includes the countries of Laos, Myanmar, Thailand, and Vietnam, allowed for the quantification of the effects of land use and cover change on landslide susceptibility (Amatya, 2021). Similarly, a 19 yearlong rainfall-induced landslide inventory of Malawi, Africa, allowed for the determination of rainfall thresholds (Niyokwiringirwa, 2023). In response to a 2015 7.8 magnitude earthquake in Nepal, the creation of a landslide inventory allowed for the analysis of landslide density and mobility values (Roback, 2017). While event-based inventories document the occurrence of landslides after a single rare event, they do not allow for the analysis of landslides in response to multiple more frequent triggers, like intense precipitation.

Landslide inventories have also been created using Light Detection and Ranging (Lidar) data. Lidar is high-resolution topographic data that is used to map elevation and create 3D models of the Earth's surface. Lidar is typically obtained by airplanes and drones although some satellites have the capability to obtain it at a low resolution. By comparing Lidar captured before and after a landslide, you can quantify how the elevation of the surface has changed and how much earth mass has been moved (Burns, 2016; Burns 2022). Lidar can only be used for the identification of landslides when pre- and post-imagery has been collected, and since acquisition is expensive, it is not frequently done over large areas. Additionally, Lidar alone cannot provide precise timing of landslides when imagery is acquired months or more likely years apart.

Purpose of PoW Inventory

This thesis presents a high-resolution landslide inventory for PoW and the smaller surrounding islands and explores some of the fundamental characteristics of these landslides. We report the number, area, and date of occurrence for landslides with a polygon inventory created

with high-resolution satellite imagery. The results demonstrate how topography, precipitation, geology, and forest stand age control landslide location and occurrence. The inventory is multi-temporal, documenting all landslides over a multi-year period. This approach enables the identification of triggers, such as specific rainfall amounts, at a later stage.

Only recently has research been conducted to connect the timing of landslides to the amount and intensity of precipitation in a location, despite understanding that spatial rainfall patterns can determine landslide distribution across a landscape (Darrow, 2022). In the future, we can connect the careful documentation of the timing and location of landslides in this inventory to rainfall datasets. By determining precipitation characteristics that do and do not trigger landslides, we can define rainfall amounts and durations (thresholds) for landslide risk. The highly accurate georeferencing of the imagery and inventory will allow us to associate mapped landslides with the relevant topographic and geologic context for comparison with landslide occurrence predictions. Historical landslide records, precipitation triggering levels, and in situ data, can be combined to develop landslide warning systems, such as the dashboard created for Sitka, Alaska, and help minimize exposure for communities during periods of extreme rainfall (Patton et al., 2023).

Study Area

Location

Prince of Wales Island (PoW) is about 40 kilometers west of Ketchikan, Alaska and at 6,675 km^2, is the largest island of the Alexander Archipelago. The island is 215 km long, 105 km wide and is slightly larger than the state of Delaware (Figure 1). The area included in this study is PoW and the smaller surrounding islands in the eastern and western direction. The study area includes the following islands: PoW, Dall, Sukkwan, Suemez, Baker, Lulu, San Fernando, Noyes, Heceta, Kosciusko, and Warren. Latitude values of the study area are between 54.50° and 56.50° and longitude values are between -131.75° and -134.00°. The total land area of the study area is over 9,000 km^2.

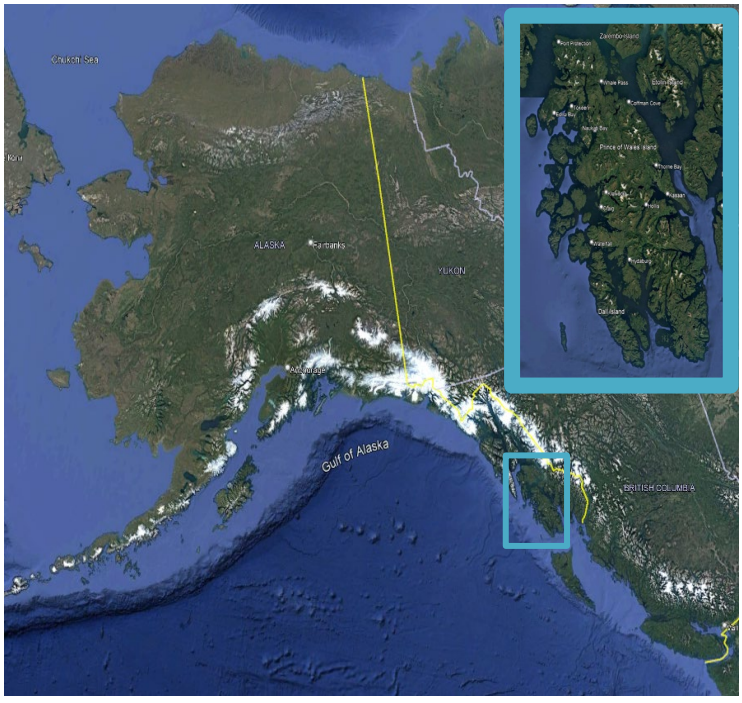

Figure 1: Map of Study Area

Image of Alaska from Google Earth Pro with a box around Prince of Wales Island (PoW). Inset: Prince of Wales Island, Alaska and the surrounding islands in Southeast Alaska.

Geology and forests

The landscape of the study area has been sculpted by Pleistocene glaciation (Swanston, 1969), tectonic activity (White et al., 2016; Elliott and Freymueller, 2020), and clearcutting (Johnson, 2000). The study area is dominated by rocks of the Alexander Terrain, a large accretionary fragment, consisting of granodiorites, greywackes, conglomerates, limestones, and sandstones (Johnson, 2000). PoW is densely forested and is dominated by stands of western hemlock, Sitka spruce, red cedar, Alaska yellow-cedar, and shore-pine (Johnson, 2000). Clear-cutting of the old-growth forests has occurred since the 1950s resulting in a mosaic of clearcuts, second growth, and old growth patches.

Precipitation and atmospheric rivers (ARs)

The mid-latitude maritime climate of the study area is characterized by high annual precipitation. Rainfall occurs year-round, but September–January are the wettest months, and the average annual precipitation is about 1.9 meters. Mean monthly temperatures stay above freezing all year. Variable snowpacks accumulate in winter months, particularly at high elevations, but most precipitation occurs as non-freezing rain in coastal and low-elevation areas (Patton, 2023).

Periods of extreme precipitation are the result of atmospheric rivers (ARs), fire-hose corridors which transport large amounts of water vapor originating in the tropics and landing in the mid-latitudes. ARs occur 8-15 days per month but account for 90 percent of extreme precipitation in SEAK and are particularly high from September to December (Sharma & Déry, 2020). The few number of AR's produce most of the extreme precipitation that the region experiences each year. The predominant direction of moisture flux during most ARs that hit Craig and Kasaan on PoW occur in the southwesterly direction (Figure 18). This pattern of

moisture encourages more orographically forced precipitation to occur on southwest facing slopes (Nash, 2024).

The only weather station with long-term precipitation records is located at the Klawock Airport (PAKW) on the western and central part of PoW at an elevation of 9.7 meters. The sole weather station does not fully represent how the weather patterns vary with the complex topography of the region and provides little real-time weather data.

Communities in the study area

Unlike many other islands and populated areas in Alaska, PoW has a large and interconnected road network. The approximately 2,400 km of roads connect the populations that are spread out throughout the island (Figure 2A and 2C). The communities of Klawock and Craig, located 15 miles apart in the central part of the island, have a combined population of approximately 1,700 people. Hollis and Kassan are located on the eastern portion of the island, and each have a population of about 30 people. Coffman Cove, in the north, and Hydaburg in the south have a population of 125 and 375, respectively. The inter-island ferry with routes to Ketchikan, runs out of Hollis, which requires that the highway across the island is clear of debris year-round for people to be able to leave the island. During the winter, flights can be unreliable with changing weather conditions while the ferry is more consistent.

Landslide Inventories in SEAK

In SEAK, the United States Forest Service (USFS) Tongass National Forest, has created and maintained a landslide inventory to document historical events. Using air photos taken every 10 years since the 1950s, the inventory has identified over 20,000 landslides in SEAK. In more recent years, the USFS has transitioned to using satellite imagery with better georeferencing. In addition, the database includes a categorization of landslide styles and mechanisms, such as

debris flows, rockfalls, or deep-seated. The Tongass inventory is a valuable resource because it identifies the general timing and location of landslides in the region and allows us to determine the spatial and temporal patterns of historical landslides.

While the Tongass inventory has a long record period and large coverage area, the methods used to create it have affected the spatial and temporal accuracy. The inventory uses air photos which are difficult to precisely georeference and consequently, decreases the spatial accuracy. A handful of landslides have an exact known date of occurrence because of community members reporting their occurrence but most landslides have an estimated date of occurrence of multiple years (~10). Additionally, since SEAK is a large region, only certain areas are remapped each year, which means that the temporal accuracy may vary depending on the location and how recently the area was mapped. Our goal is to use high-resolution Planet imagery to identify the location and timing of landslides over the past 15 years which will improve the understanding of landslide occurrence from that provided by the Tongass inventory in the study area.

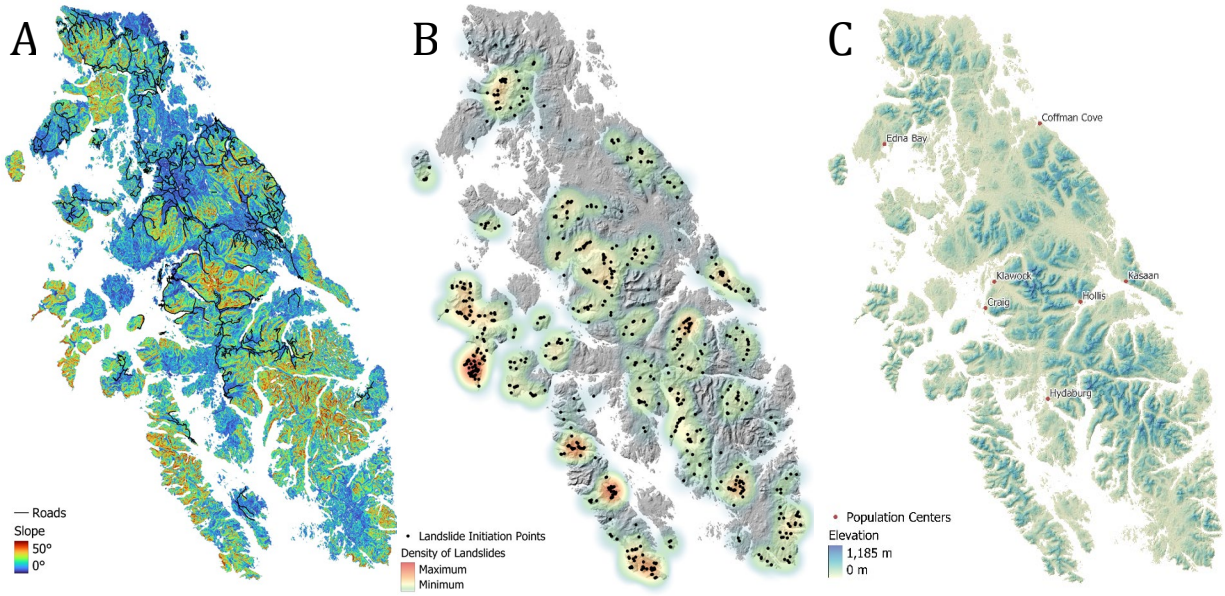

Figure 2: Various maps of the study area showing:

a slope and road network, **b** density of landslide initiation points, **c** elevation and population centers

Methods

To map and identify landslide occurrences we used high-resolution and high-quality satellite images collected between 2009 and 2023 by Planet. We examined pre- and post-event images that were orthorectified and georeferenced to visibly identify precipitation triggered landslides. After identifying landslides within the constraints of our study area, we compiled an inventory with a series of geospatial attributes for each landslide.

Between the study period of 2009 and 2023, there was variable resolution of Planet imagery. The ground sampling distance (resolution) ranged from 3- to 5-meters because there were two different types of satellites being operated. RapidEye is a constellation of five satellites that operated from 2009 to 2020 with 5-meter resolution. PlanetScope is a constellation of approximately 130 satellites with 3-meter resolution and an advertised daily revisit time (Planet, 2024). We used RapidEye images from 2009 to 2015, a combination of RapidEye and PlanetScope images from 2014 to 2019, and only PlanetScope images from 2020 to 2023.

The types of images that the RapidEye and PlanetScope satellites produced also vary across the period of the study. The RapidEye satellites produce two types of products: Scene and OrthoTile. We specifically use OrthoTile images because they have a higher resolution (5m) than Scene images (6.5m). Images processed as RapidEye and OrthoTile images are taken from the same satellite on identical days and thus, we do not miss any imagery by only using OrthoTile images. OrthoTile products are 25 x 25 square kilometers tiles generated from a set of consecutive scenes within a strip. In comparison, PlanetScope imagery is only available as an individual framed scene within a strip, captured by the satellite in its continuous line-scan of the Earth. Scenes within a strip are overlapping and not organized by any tiling grid system. The length of the strips is constrained by the size of the study area.

For every year between 2009 until 2023, we gather imagery from approximately July until September within the study area to understand where and when landslides are occurring on a yearly basis. Due to the cloudy and rainy nature of the region, clouds and shadows often obstruct land, but the clearest images are frequently obtained during late summer, specifically August and September. Therefore, imagery from multiple dates during the late summer are downloaded. We then create a new QGIS project (EPSG: 32610) for each year, import the corresponding satellite imagery, and confirm that there is full cloud-free coverage for every part of the study area.

Beginning with 2009 imagery, when Planet imagery is first available, we begin the process of manual mapping landslides in QGIS. First, we overlay a 10km x 10km grid over the study area, set the computer screen height to one grid cell, and scroll through each cell to identify landslides (Figure 1). We use a grid to ensure we are using a consistent resolution. Landslides are most easily recognized visually and via changes in spectra associated with vegetation loss, but landslides are more difficult to recognize above tree line. The difficulty in identifying landslides in areas without vegetation or snow may bias observations in these settings. The perimeter of each landslide is traced as a closed polygon feature and a point feature is placed equidistant from the top, left, and right sides of every landslide polygon to represent an initiation point. The latitude and longitude of every initiation point is calculated using the field calculator function. In the years following 2009, this process of identifying new landslides is repeated. We lay all previously identified landslides on top of each year of satellite imagery to ensure only new landslides are included. Afterwards, we dug back through the inventory to determine a narrower timing of landslide occurrence.

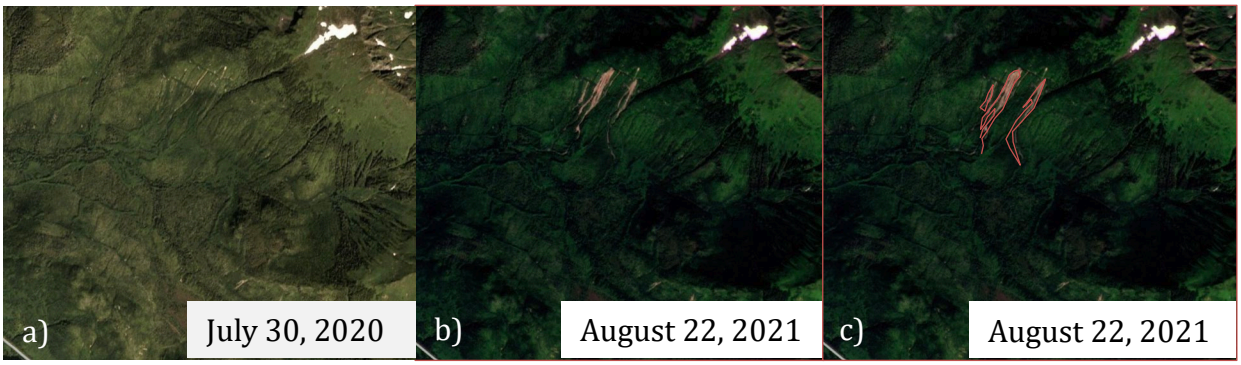

Figure 3: Example representing the process of identifying occurrence dates of landslide events

a PlanetScope image before the event; **b** PlanetScope image after the event, with the indication of landslides; **c** Red polygons show the manually mapped landslide polygons.

For our study, we determined that representing landslide outlines as polygons was the most accurate method. Other studies that are prioritizing immediate response and recovery efforts have opted to map landslides as points (Kargel et al., 2016). Since we are mapping years after landslides had occurred, taking the time to create polygon outlines allows us to conduct the analysis of topographic, climatic, and spatial characteristics of landslides across their whole shape, from the head to the toe. Additionally, we determined that creating polygons around the head scarp, where the landslide initiates from, would be too difficult to determine from the resolution of satellite imagery used since there is no visible differentiation of the end of the scarp (Roback, 2017). The head scarp polygon is recognizable in post-landslide Lidar but not in satellite imagery. Therefore, we opted for an initiation point inside each polygon outline.

Following mapping of landslides in plain view with approximately a one-year time frame between images, we went back through the inventory to determine the most accurate landslide event date. We enter the latitude and longitude for each initiation point on the Planet Explorer website and constrain the date. For example, a date filter of July 2020 to September 2021 reflects a landslide that was identified with late fall 2021 imagery in QGIS. We narrow down the landslide timing using imagery that was unobstructed by clouds or shadows. The last available

pre-event image is considered the “not seen” value and the date of the first available post-event image is the “seen” value. The number of days between the “not seen” and “seen” values are the “date difference” values. We calculate the halfway date between the “not seen” and “seen” values as the “middle date” value. Landslides mapped with 2009 imagery were lacking a “not seen” value because of imagery availability constraints and are not included in the final inventory. Some time periods suffered from a lack of cloud-free images or snowpack at high elevations, which made it more difficult to determine accurate timing in those settings. Additionally, the frequency of images improved throughout 2009 until 2023, which makes it possible to more accurately determine the timing of landslides as the inventory progresses.

Following the identification of landslides in plain view, we calculate geospatial statistics using the 5-meter Digital Terrain Model (DTM) GeoSAR Interferometric Synthetic Aperture Radar (IFSAR) topographic data collected in 2012 by the Alaska Department of Geophysical and Geological Surveys. Higher-resolution Lidar data collected in 2017 and 2018 did not cover the southern portion of PoW and our analysis required consistent same-resolution coverage. In QGIS, we merged all the IFSAR tiles within the study area and created slope, elevation, and aspect layers using the Raster Terrain Analysis function. Then, we determined the slope, elevation, and aspect values at each initiation point using the Point Sampling function.

Topographical information was calculated using the Zonal Statistics Toolbox in QGIS which helps us determine how far the landslide travels. The lowest and highest elevation values within each polygon were calculated by setting the statistics to ‘minimum’ and ‘maximum’. The difference between the lowest and highest elevation values is the landslide height.

Geometric attributes of each polygon were calculated using the field calculator function to determine the size of each landslide. We calculated the area, length, and width of each

landslide. Mobility values were calculated for each landslide by dividing the height by the length of the polygon

The spatial relationship between the location of landslides and the corresponding geologic units is useful to see if certain types of rocks have more landslides occurring in them (Table 1). To determine this, we performed a spatial merge between the landslide initiation points and a combined geologic map of Alaska with unit descriptions (Wilson, 2015) and then categorized the units into seven rock categories based on their descriptions: calcareous, felsic volcanic, mafic volcanic, felsic intrusive, mafic intrusive, clastic sedimentary, and metamorphic (excluding marble). This process was completed in Python using the GeoPandas library

The relationship between the age and type of forest at each landslide location was analyzed to see if how old the forests have an effect on when landslides occur. We completed a spatial merge between landslide initiation points and the United States Forest Service Tongass National Forest Cover Type ALL layer from the State of Alaska Geoportal. We determined whether the landslide is in a forested or non-forested area, whether the area has been timber harvested in the past, and the date of the harvest. Then we calculate the difference between the date of timber harvesting and the middle date of landslide occurrence to determine the number of days it took for landslides to occur after harvest. Landslides that are in non-forested areas or have not been harvested have no date representing the difference between the harvest and landslide occurrence.

The spatial relationship between roads and landslide location is important to understand how close landslides are getting to traffic corridors that might shut down transportation routes. We gathered OpenStreetMap data within the study area and calculated the Euclidean distance between the landslide initiation point and the nearest road. Some roads and trails may not be

included in OpenStreetMap because they are not maintained or used only seasonally. This may cause an underestimate of distance between landslides and travel corridors in this study.

To ensure that only landslides, and not similarly looking features were included in the inventory, a series of data quality control activities were completed. We are mostly concerned about natural and man-made activities, primarily clear-cutting and road construction, producing comparable vegetation changes to landslides, might accidentally be included. First, each year of imagery in QGIS was scrolled through two times with the grid system to ensure no landslides were missed. Second, we overlaid the inventory polygons and initiation points on the elevation and hillshade profiles to ensure the point had been placed at the higher elevation end of the landslide. This process also helped us delete any polygon that had a difference in elevation less than 20 meters from the top to the bottom. Third, we examined each landslide to ensure that the polygon outlines were representative of the landslide geometry. Finally, after determining the most accurate landslide event date with pre and post imagery, every landslide was reviewed a second time, to ensure the date assignments were accurate.

To compare landslide timing with precipitation levels, we summarized daily data collected from the Klawock Airport, accessed via MesoWest from the University of Utah, between the beginning of 2009 and the end of 2023. We calculated the monthly and yearly averages using NumPy in Python.

Data Name	Data Source	Date
Planet Imagery	Planet	2009-2023
DEM - IFSAR	Alaska Department of Geological and Geophysical Surveys	Collected 2012
Geology	Wilson, et al. Geologic map of Alaska: U.S. Geological Survey Scientific Investigations Map 3340.	Published 2015
Forest Stand	USFS Tongass National Forest Cover Type ALL	Updated 2024
Roads	OpenStreetMap	Downloaded 2024
Precipitation	MesoWest	2009-2024

Table 1: Names of data and sources used to analyze spatial relationships of landslide inventory

Results

Annual and seasonal trends

We have identified 766 landslides within the study area, spanning from 2009 to 2023. On PoW alone, we observed 434 landslides. The highest concentration of landslides occurred in 2020, when 160 landslides were recorded (Figure 4). The lowest rates of landsliding were observed in 2018, 2017, and 2022, with 5, 10, and 15 events, respectively. We do not observe a clear relationship between annual precipitation and the number of landslides (Figure 4). Although the largest number of landslides occurred in 2020, which had only 1.4 meters of cumulative annual precipitation, the average annual precipitation during the study period (January 2009 to December 2023) was 1.9 meters.

A general pattern of higher cumulative precipitation is evident in the first portion of the study period, with lower cumulative precipitation in the latter half. From 2010 to 2017, the average annual precipitation was 2.1 meters, whereas from 2018 to 2023, it dropped to an average of 1.4 meters. Additionally, an average of 55 landslides occurred per year from 2010 to 2017, compared to 52 landslides per year from 2018 to 2023. We exclude the year 2009 from this analysis due to the limited availability of imagery, which began in June. This suggests a slight decrease in precipitation following a corresponding decrease in landslides over the study period, but it does not fully explain landslide occurrence in relation to precipitation. While one might expect that years with higher cumulative precipitation would correlate with more landslides, this trend does not hold. The intensity and duration of storms, particularly the occurrence of atmospheric rivers (ARs), may better explain the observed pattern (see Discussion).

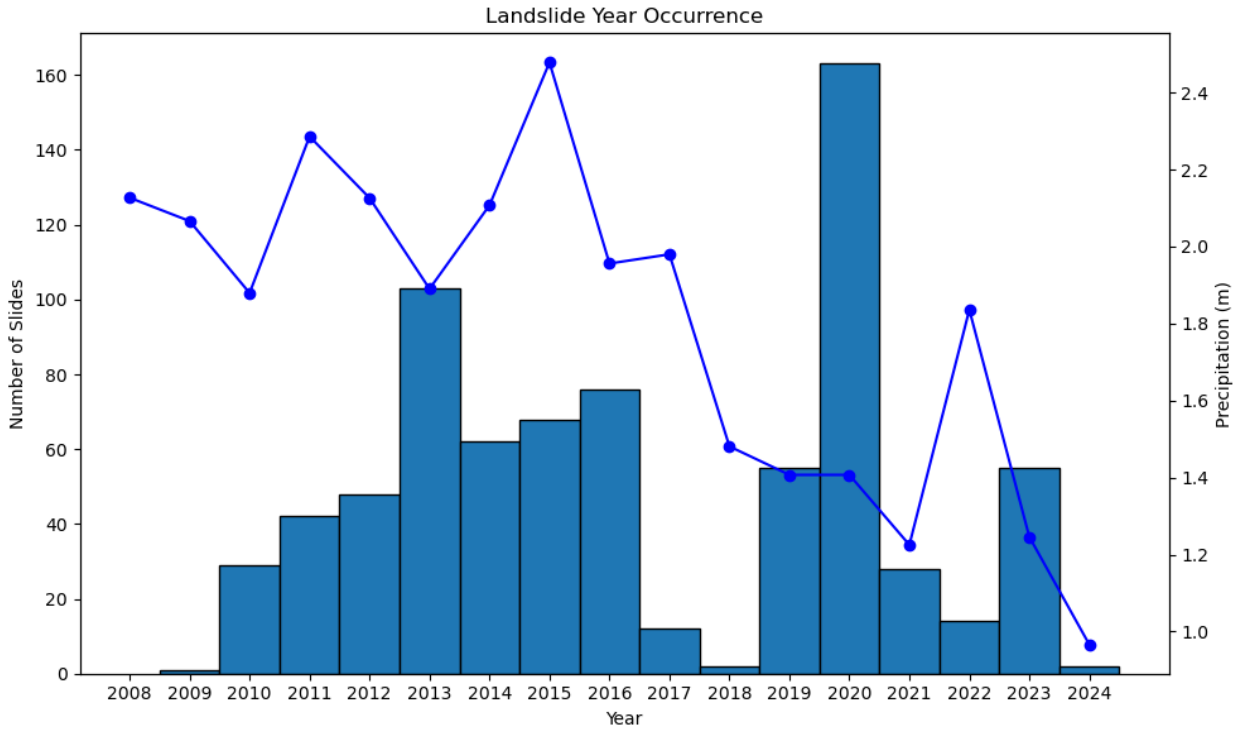

Figure 4: Distribution of landslide timing and cumulative precipitation by year, using the middle date value.

The majority of landslides occurred in the latter months of the calendar year, from August to December (Figure 5). The difference between the landslide season and the non-landslide season is stark and consistent with both monthly precipitation data from a weather station on the island and atmospheric river patterns (Nash, 2024). From January to July, fewer than ten landslides occurred per month (Figure 5).

To visualize the seasonality of landslide occurrence alone (Figure 5) we excluded landslides with a time precision of more than 90 days between the “not seen” and “seen” dates to avoid skewing the results with landslides that were difficult to identify due to unclear imagery. For instance, if a landslide was not visible in an October image but appeared in a March image of the following year, the middle date (used in this analysis) would fall between late December and early January. This issue was common, particularly for the months of January, February, and March, when satellite imagery was often obstructed by clouds. By only including landslides with

a time precision of less than 90 days, we ensure that the month of landslide occurrence is accurately represented. As a result of this approach, it is possible that landslides with a timing precision of 30 to 90 days may have occurred in adjacent months, which could slightly alter the observed seasonal trend.

The average monthly precipitation levels follow a seasonal pattern similar to landsliding. From January 2009 to December 2023, the highest average rainfall occurred in September, October, and November, with 12.6 mm, 11.5 mm, and 11.7 mm, respectively (Figure 5). Even in the summer months, the region still experienced notable precipitation, averaging 5.6 mm per month. To determine if landslides occurred in January and February—when precipitation levels were in the 75th percentile, but landslide records are absent from the dataset—we would need to expand our methodology to better detect landslide timing.

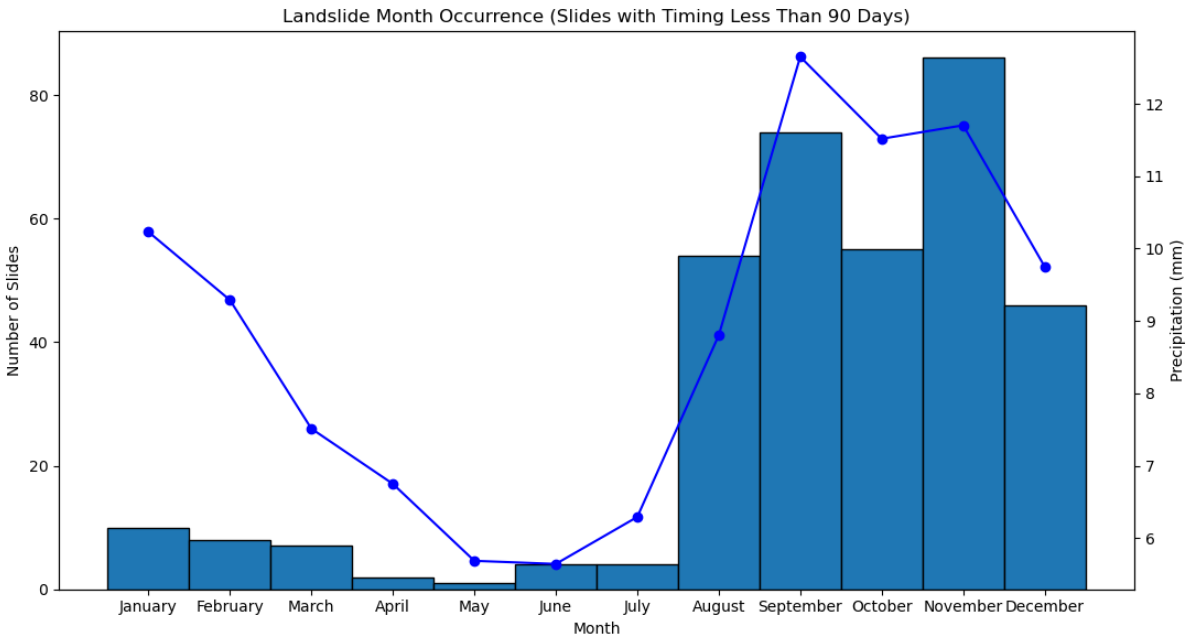

Figure 5: Distribution of landslide timing and cumulative precipitation by month, using the middle date value.

Resolution of timing

The precision of landslide timing identified in this study was determined by calculating the difference between the "not seen" and "seen" dates. Of the 766 landslides in the inventory, 3.5 percent have a timing precision of less than 7 days, 27.5 percent have a precision of less than 30 days, 19.5 percent have a precision of less than 6 months, and 46.1 percent have a precision of less than 1 year (Figure 6).

The resolution and frequency of satellite imagery influence the precision of landslide timing. Landslides with a timing precision of less than 150 days largely occurred after 2019, when we switched to using PlanetScope imagery. With the introduction of PlanetScope and the discontinuation of RapidEye, the number of satellites increased from 5 to 130, and the resolution improved from 5 meters to 3 meters. As satellite imagery quality improved, we were able to more accurately determine the timing of landslides.

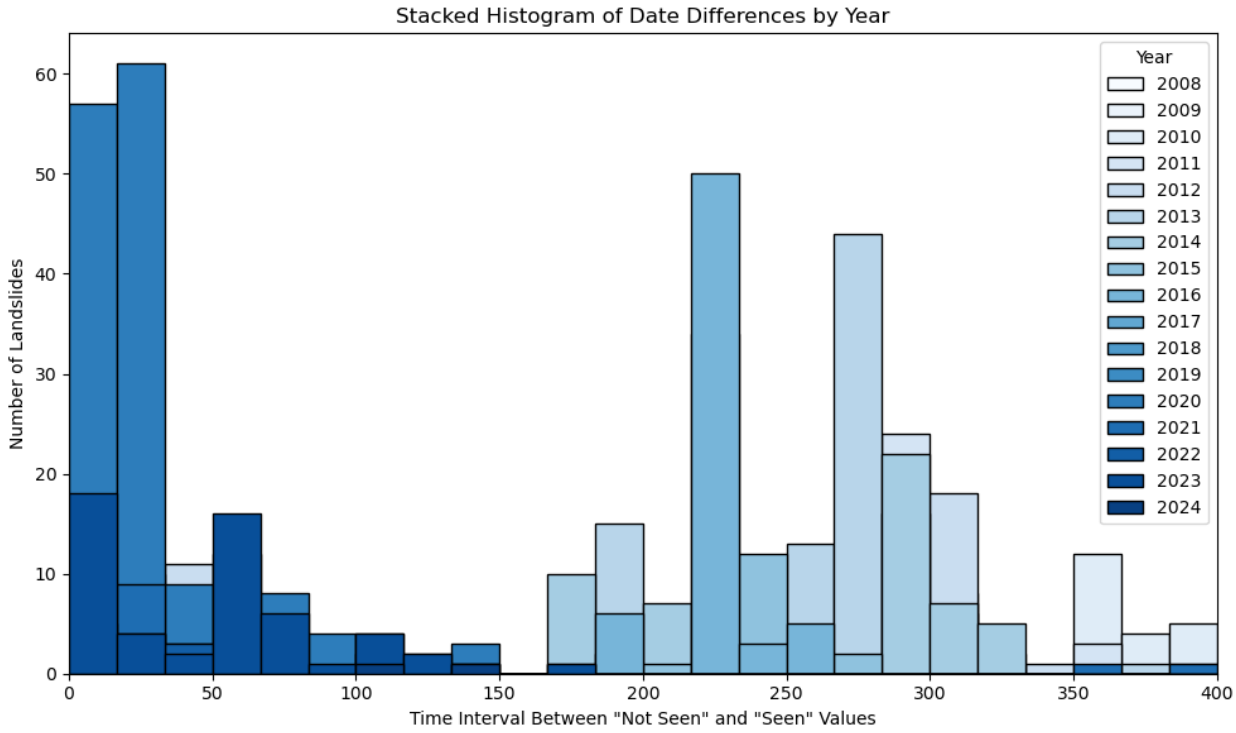

Figure 6: Distribution of precision of landslide timing as a function of year of occurrence.

Landslide number and area-frequency statistics

We have identified 766 landslides, covering a total area of 7.8 km². We examined the area-frequency distribution of the PoW landslide inventory by plotting a kernel density estimate. The frequency distribution of individual landslide areas peaks at approximately 6,300 m² (Figure 7). The smallest landslides detected in our inventory have areas smaller than 10^1 m^2, while the largest landslides are less than 10^5 m^2.

The right-skewed nature of the landslide area distribution indicates that a greater number of small landslides were observed compared to large ones (Figure 7). This skew suggests that the methods and imagery resolution used in mapping favor the detection of small landslides (Stark and Hovius, 2001). Large landslides are less frequent because they require the exceedance of stability thresholds and the combination of multiple factors, including steep slopes, large amounts of precipitation, and more susceptible geology.

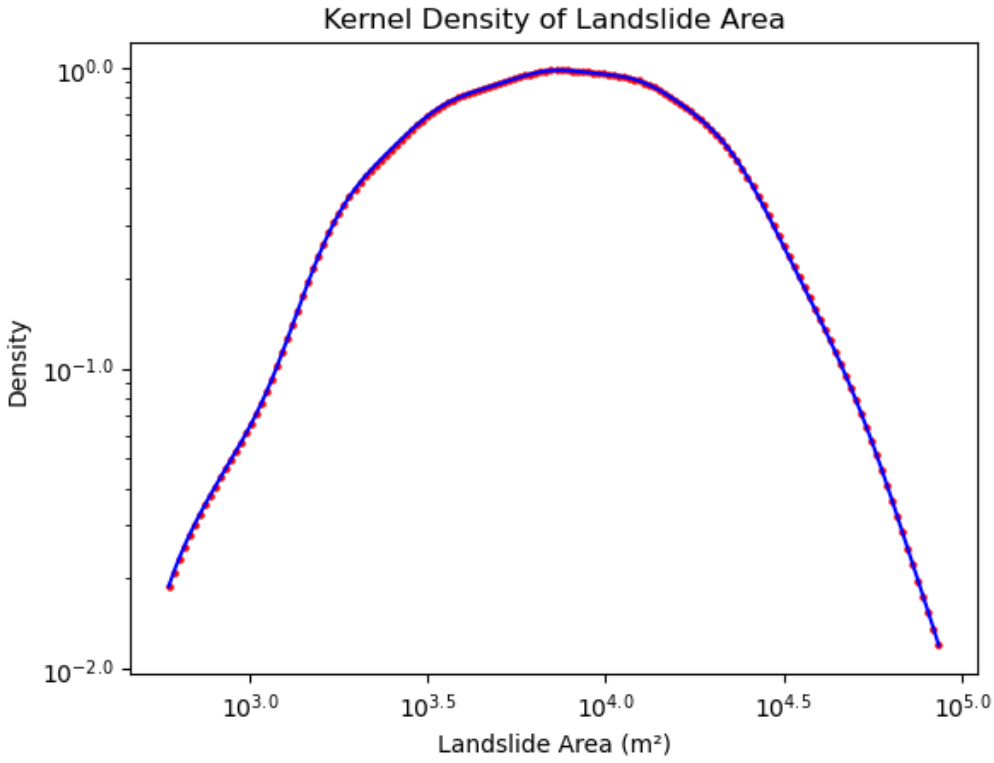

Figure 7: Distribution of landside area density on a log scale.

Mobility values

To quantify the runout of landslides, we analyzed mobility values as a function of slope to estimate how the height drop relates to the runout length ratios (H/L). The H/L ratio is suggested to represent the frictional characteristics of the landslide mass and the surface it overrides (Heim, 1932). Debris flows typically exhibit low H/L values (0.1 to 0.3), indicating small drop heights relative to their long runouts whereas larger rockslides tend to exhibit H/L values >0.5 (Iverson et al., 2015).

Most mapped landslides in my inventory have H/L ratios close to 0.5, indicating higher than values for typical mobility , which are typically reported as 0.1-0.5 (Griswold and Iverson, 2008) (Figure 8). Debris flows typically have values of 0.1-0.5 Interestingly, landslides on steeper slopes tend to be less mobile (larger H/L ratio) than those on shallower slopes (smaller H/L ratio). Landslides in the inventory on slopes less than 25° have mobility values close to 0.4,

while landslides on slopes between 25° and 45° have a typical mobility value of 0.5. Landslides on slopes greater than 45° have mobility values around 0.6. One might expect landslides on steeper slopes to be more mobile due to the associated higher potential energy.

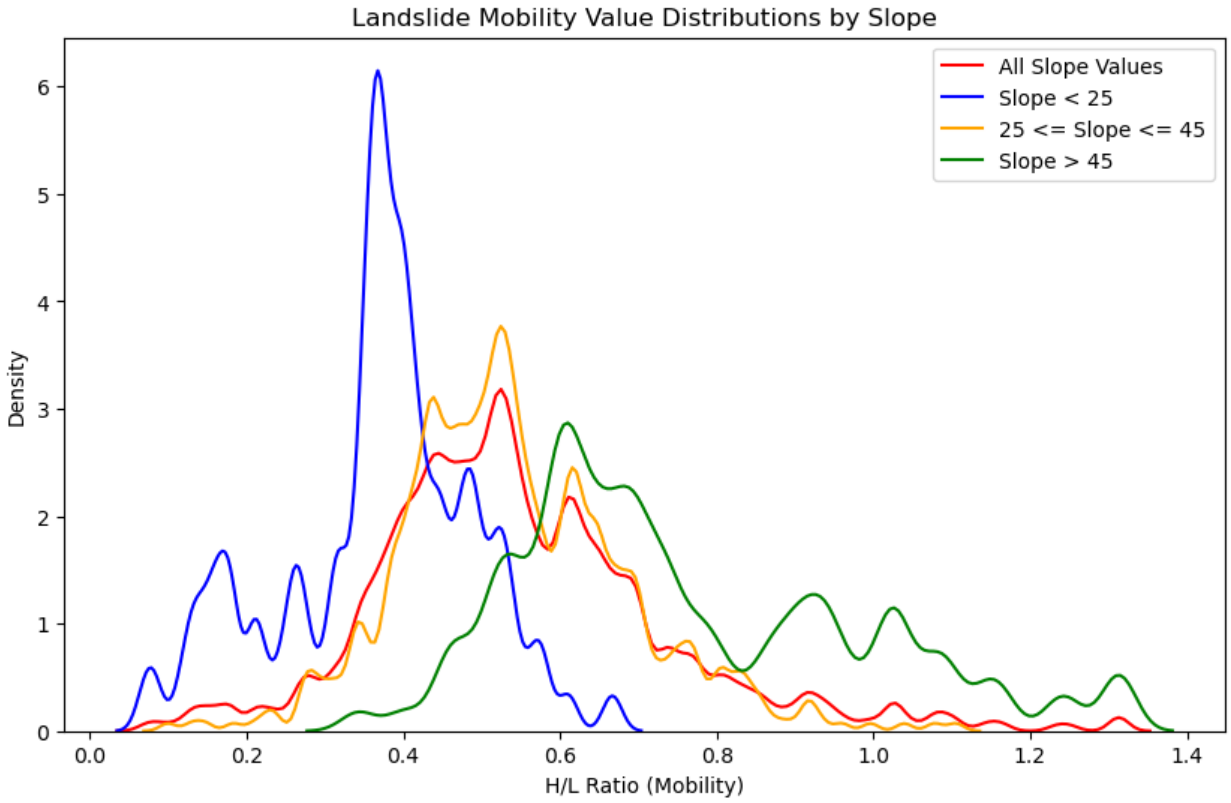

Figure 8: A density distribution function of mobility values, separated by slope ranges

The ranges are less than 25°, between 25° and 40°, and greater than 40°. Mobility values are calculated by dividing the height difference of the landslide by the length of the landslide.

Landslide density: relation to slope, elevation and aspect

To assess how terrain that experiences landslides differ from non-slide terrain, we compared the slope, elevation, and aspect of landslides in the inventory with these metrics for the total study area. To do this, we generated 100,000 random points across the study area to calculate slope, elevation, and aspect values, ensuring a comprehensive representation of the landscape.

We observed that 80 percent of all landslides occur on slopes between 25° and 45° (Figure 9). In the study area, only 25 percent of the land has slopes in this range, suggesting that landslides are restricted to areas with sufficiently steep slopes, constituting of only a quarter of the study area. Landslides occurring on slopes less than 25° or greater than 45° account for only about 20 percent of the total landslides identified.

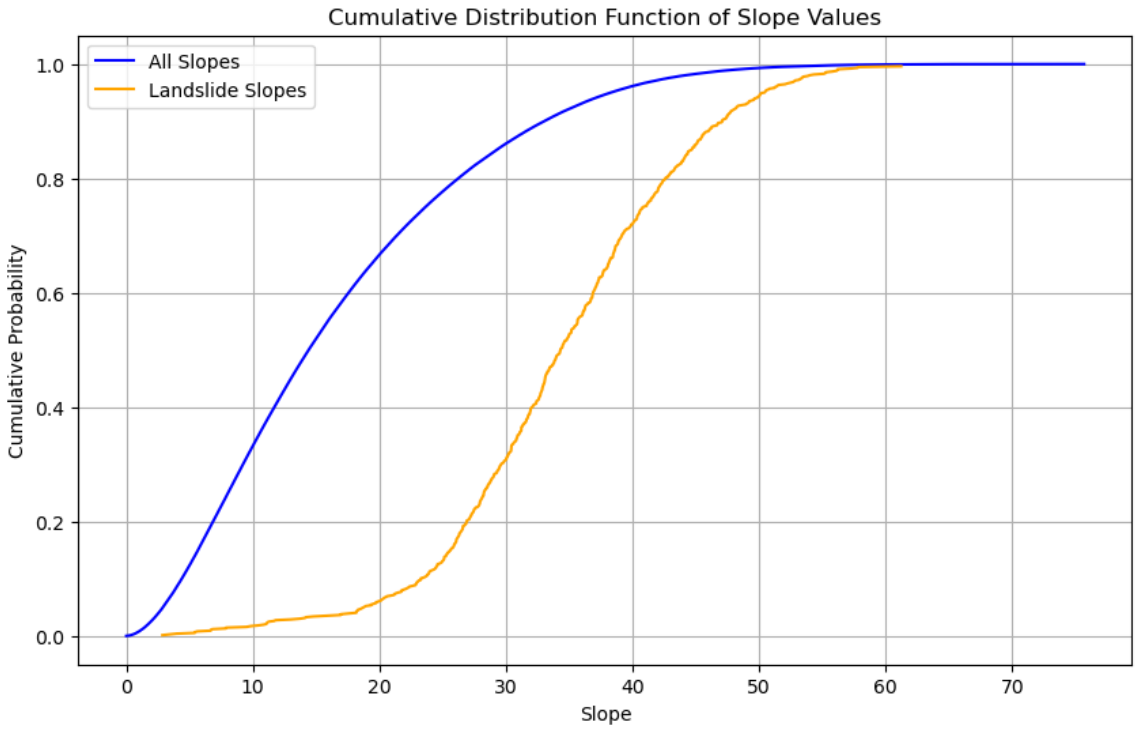

Figure 9: A cumulative distribution function of landslide slopes compared to all slopes in the study area.

We also found that all landslides occur at elevations below 700 m, while elevations in the study area span to 1,200 m (Figure 10). Approximately 80 percent of landslides occur at elevations below 350 m, and about 80 percent of all land in the study area is at elevations below 350 m. Since only 20 percent of landslides occur between 350 m and 700 m, we conclude that landslides are less frequent at higher elevations. At high elevations, the landscape often lacks vegetation, making it harder to detect landslides creating a bias in the inventory data.

Furthermore, most landslides occur at lower elevations, where communities and roads are located, such that people in these areas are more likely to be affected by landslides.

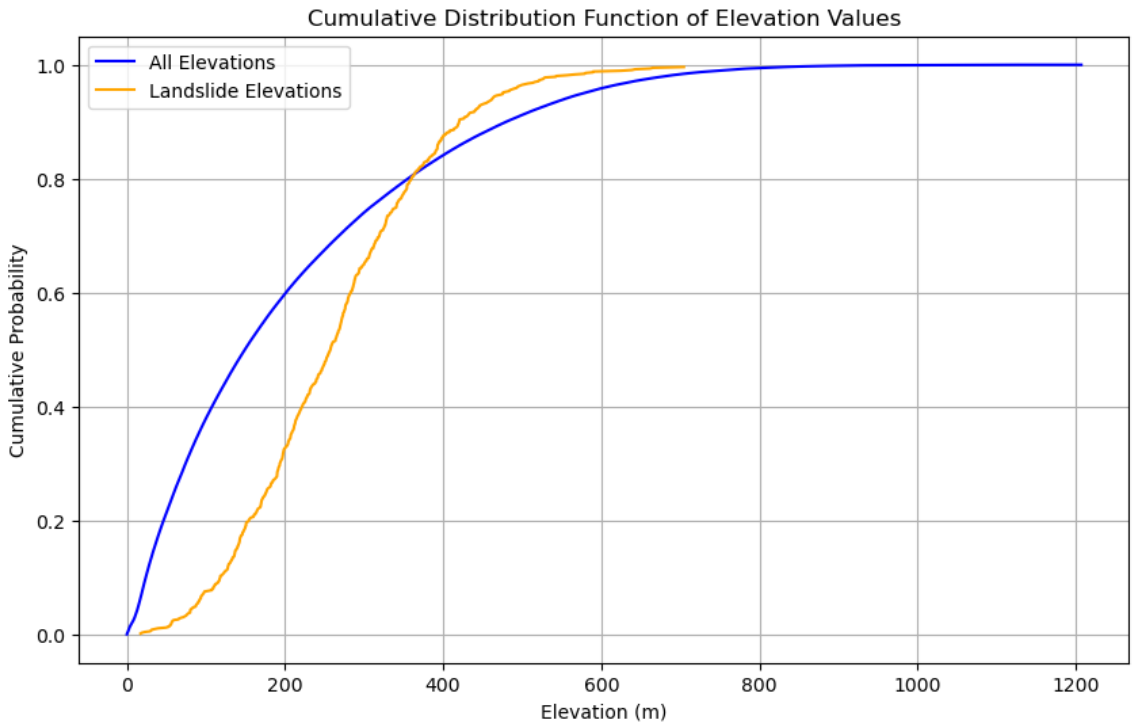

Figure 10: A cumulative distribution function of landslide elevations compared to all elevations in the study area.

The aspect (or downslope orientation) of hillslope initiation zones and is correlated with patterns and directions of storms, both of which impact landslide location. The study area contains more western- and eastern-facing slopes, yet landslides primarily occur on southern-facing slopes, regardless of slope steepness (Figure 11). If landslide occurrence were simply a function of the landscape's aspect, we would expect a higher density of landslides on eastern and western slopes, which is not observed here.

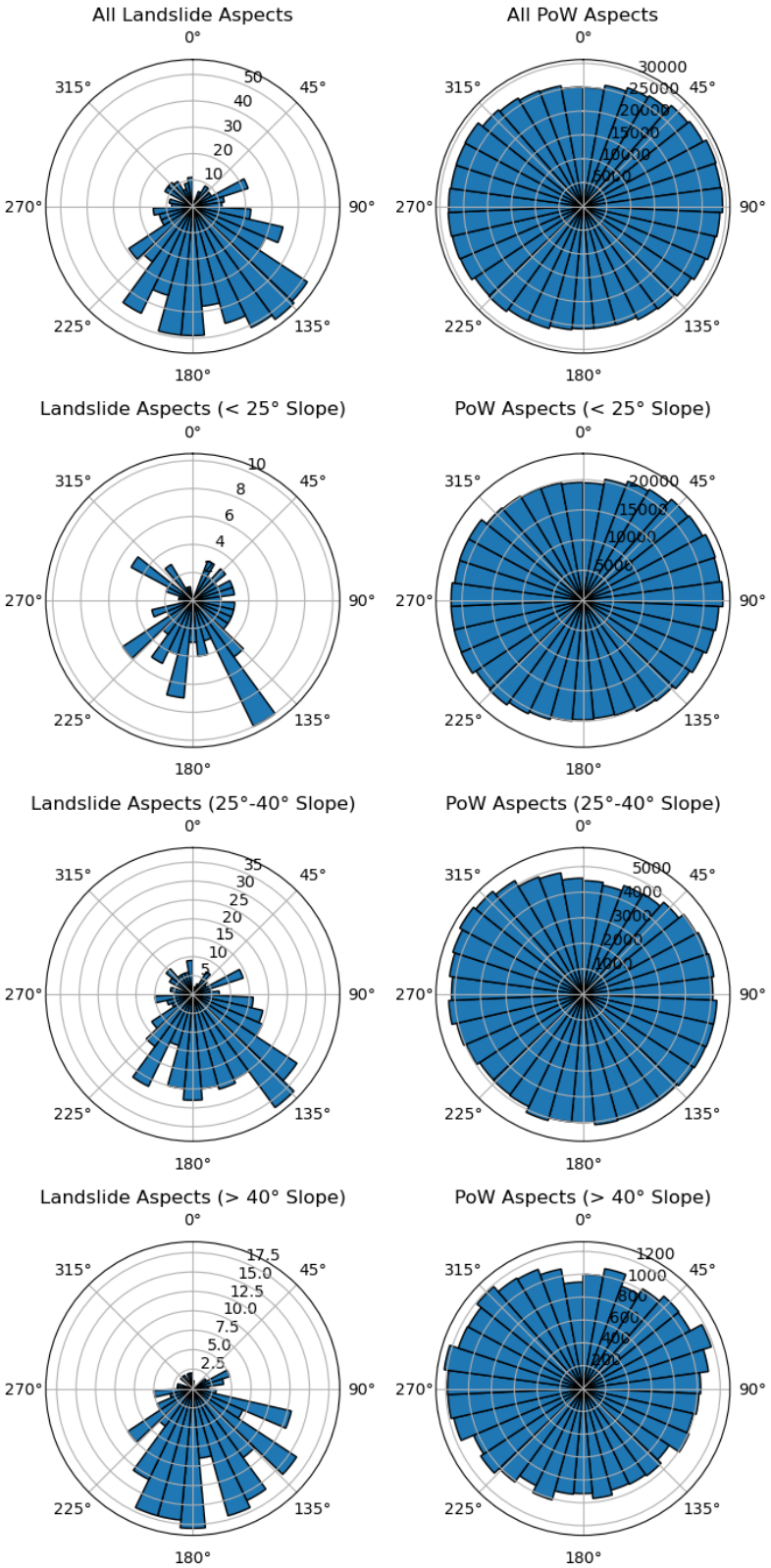

Figure 11: A rose plot of landslide aspect compared to the study area aspect, separated by slope categories

Slope categories are all slopes, less than 25°, between 25° and 40°, and greater than 40°.

Landslide density: relation to forest stand age

The history of clearcutting and forest harvest on PoW dates to the 1950s and continues to the present day. We analyzed the time between the reported harvest date and landslide occurrence to determine how long it took for landslides to occur post logging.

To determine the relationship between forest stand age and landslide location, we compared our inventory with the Tongass National Forest Cover GIS layer. Of the 766 landslides, 83 percent (N = 632) occurred in forested areas, while 17 percent (N = 134) occurred in non-forested areas. Of the landslides in forested areas, 21 percent (N = 132) occurred in previously harvested regions. Of the landslides in harvested areas, 79 percent (N = 132) had a recorded harvest date.

Our analysis reveals that landslides in harvested regions typically occurred 20 to 30 years after clearcutting (Figure 12). This is longer than the time lag between harvest and landslide occurrence observed in other regions (Schmidt, 2001; Johnson, 2000). For example, after a large storm in October 1993, over 300 landslides were triggered on PoW, 50 percent of which occurred in clearcuts harvested just one year prior (Johnson, 2000). Similarly, in the Oregon Coast Range, landslides occurred 10 years after clearcutting (Schmidt, 2001). Our findings suggest that landslides in this study area take longer to occur after clear-cutting compared to other regions, which may reflect the influence of logging roads and related harvest activities.

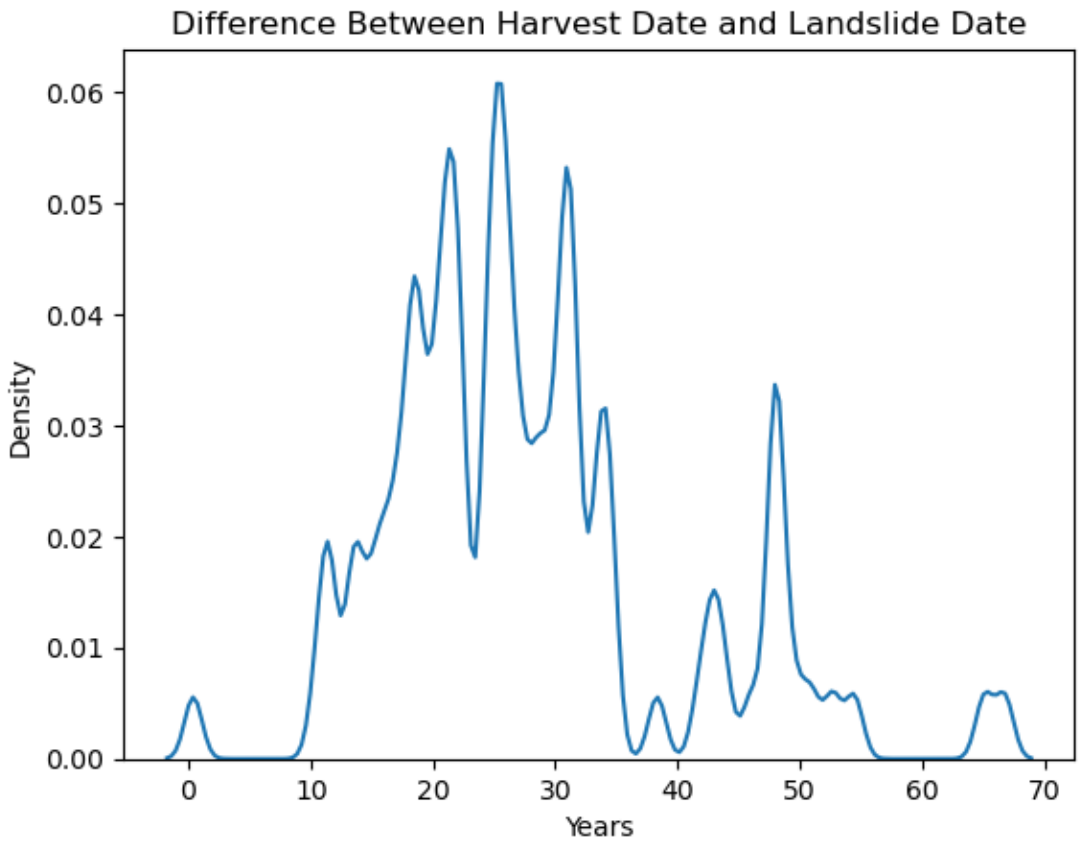

Figure 12: A density distribution function of the time difference between forest harvest and landslide occurrence

The difference is calculated using the middle date between the last day "not seen" and the first day "seen."

Landslide density: relation to roads

The distance between landslides and roads is important for evaluating their potential impact on transportation and infrastructure. Landslides in the study area range from 0.01 km to 37 km from the nearest road (Figure 13). About 50 percent of landslides are less than 8 km from the nearest road, and 80 percent are less than 17 km away (Figure 13, inset). This proximity analysis helps assess how landslides affect communities on the island, especially since they are often spatially distant and connected only through a few main highways.

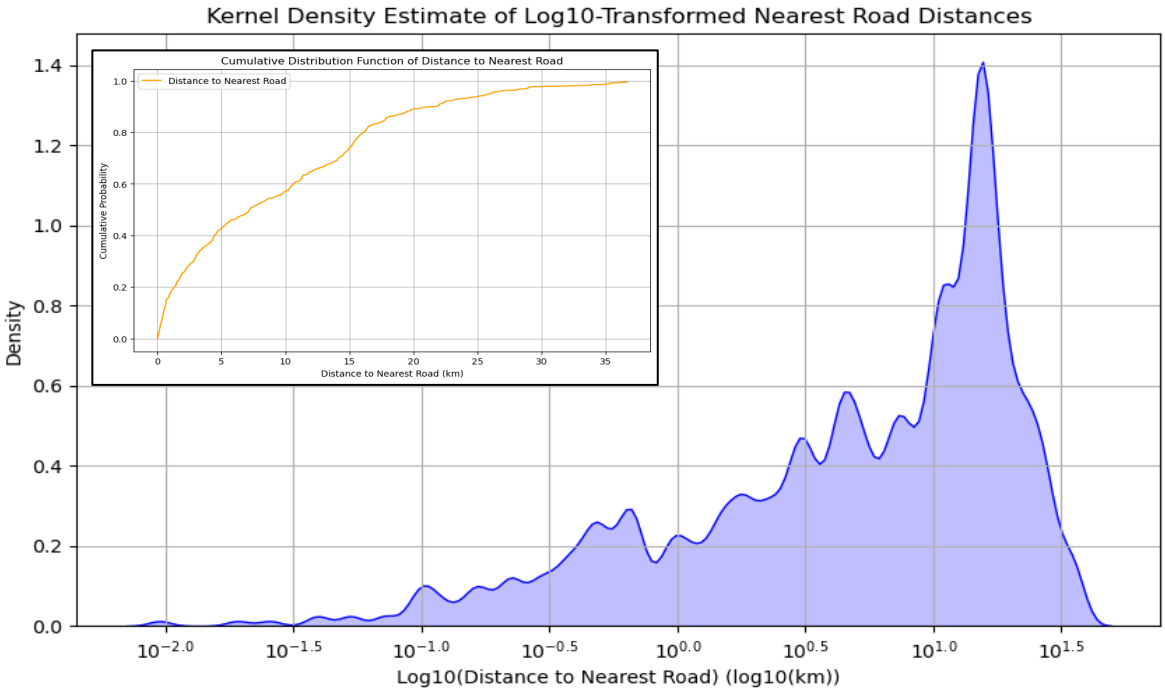

Figure 13: A density distribution function of the Euclidean distance between landslides and the nearest road

Inset: a cumulative distribution of distances between landslides and the nearest road.

Landslide density: relation to lithology

Landslides are distributed across volcanic, intrusive, sedimentary, and metamorphic rocks. We observe a higher proportion of landslides in volcanic, intrusive, and metamorphic rocks compared to their representation in the total study area (Figure 14). For example, approximately 25 percent of landslides occur in intrusive rocks, even though this rock type only represents 15 percent of the study area. Conversely, landslides in sedimentary and calcareous rocks are overrepresented relative to their areal extent in the study area.

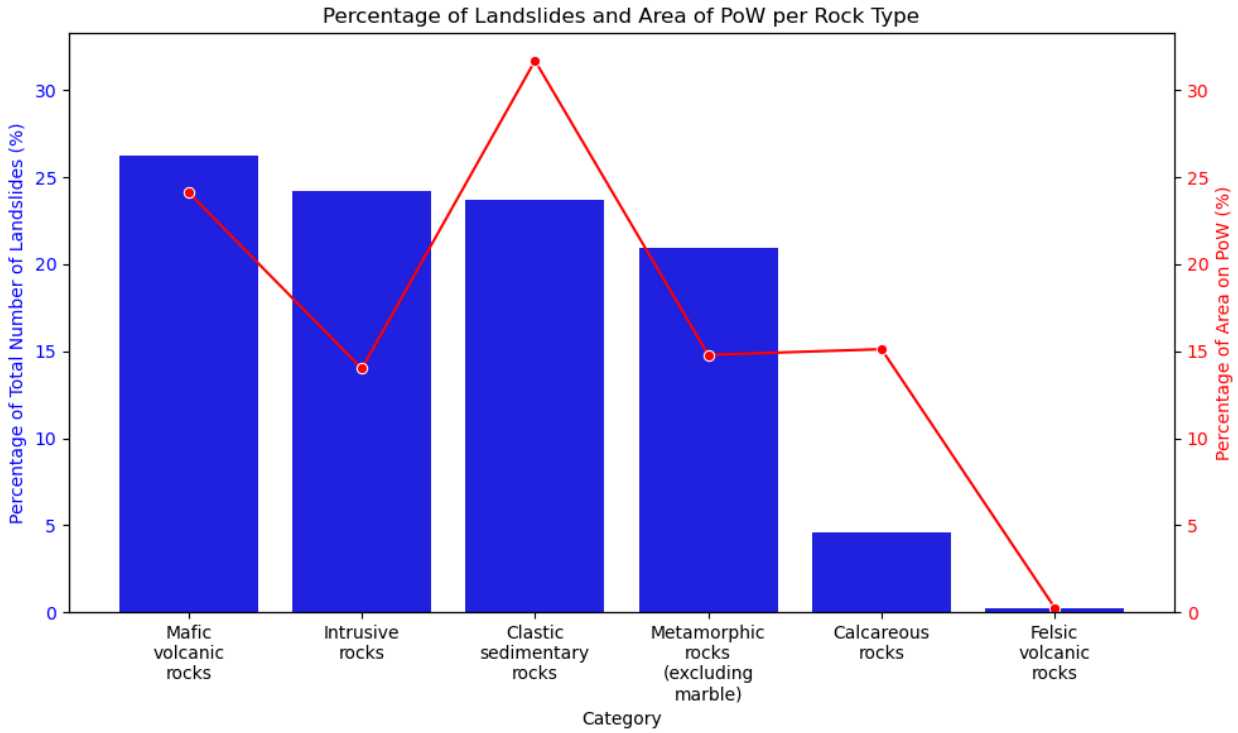

Figure 14: Distribution of landslide frequency and the percentage of the study area by geological units.

Large landslides are most common in metamorphic rocks and least common in felsic volcanic rocks (Figure 15). The median landslide area in metamorphic rocks is about 10,000 m², compared to 7,500 m² for intrusive, sedimentary, mafic volcanic, and calcareous rocks. Felsic volcanic rocks have few landslides

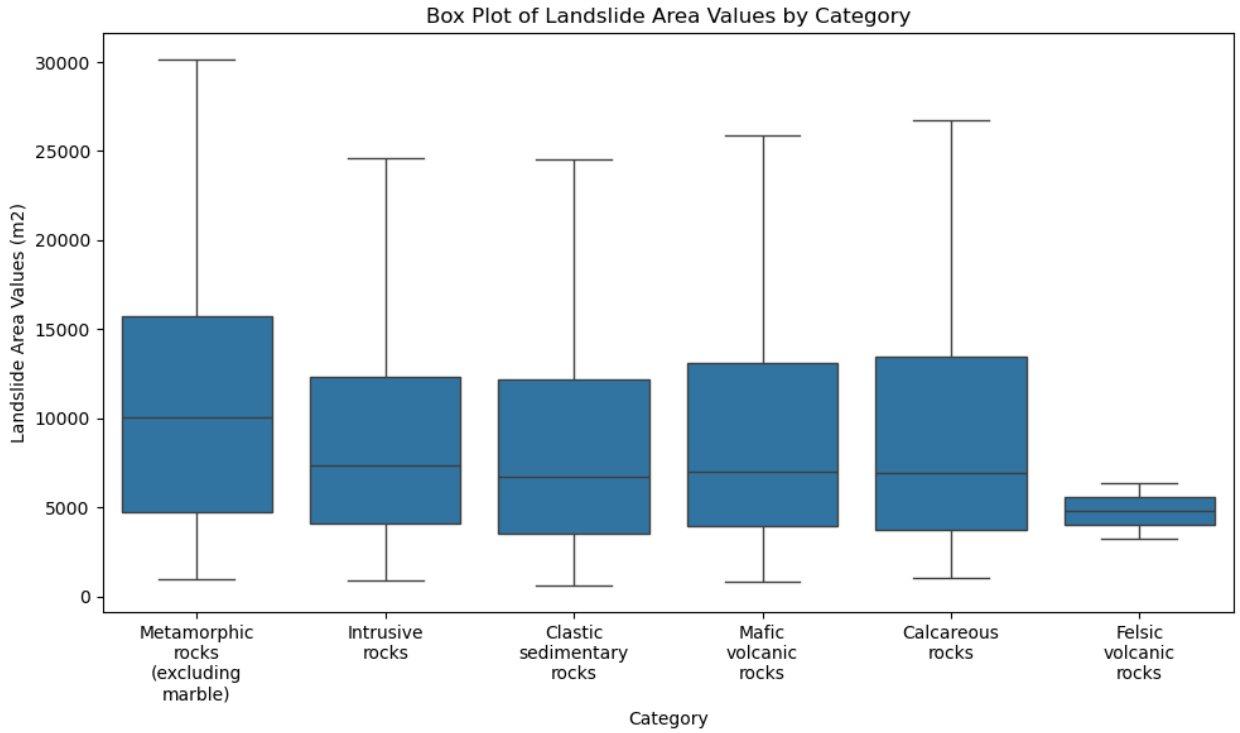

Figure 15: Distribution of landslide area (m^2) by geologic units.

Sedimentary, calcareous, and felsic volcanic rocks occur at lower elevations (median ~125 m), while metamorphic, intrusive, and mafic volcanic rocks occur at higher elevations (median ~200 m) (Figure 16). In general, landslides occur at higher elevations than the landscape, regardless of rock type (Figures 10 and 16).

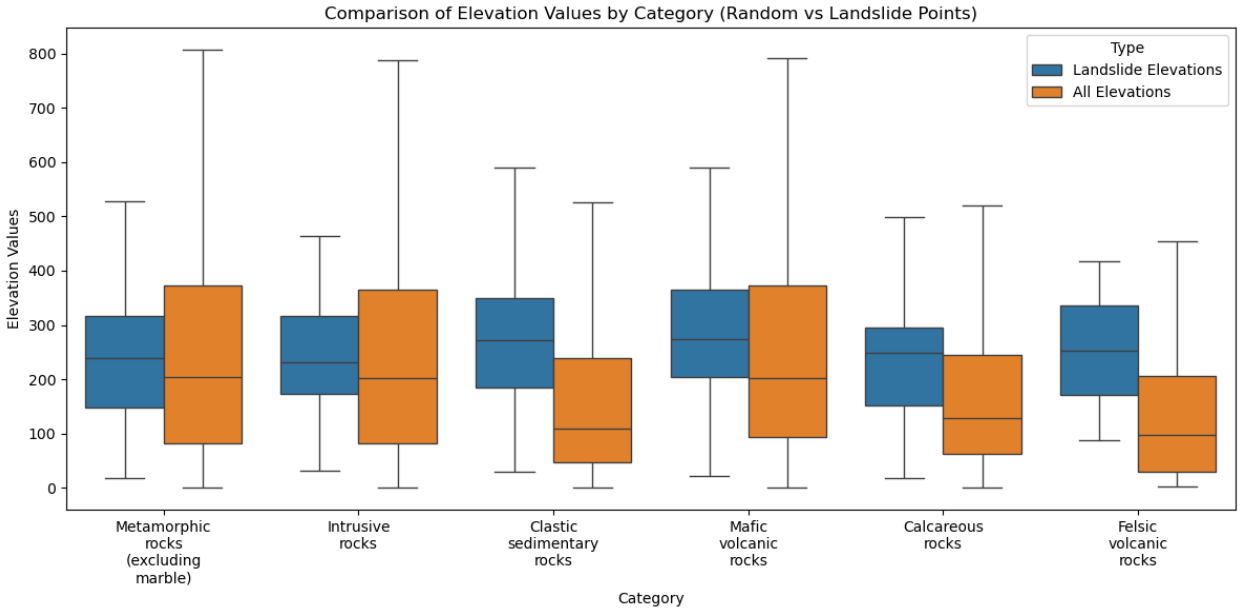

Figure 16: Distribution of landslide and study area elevation values by geologic units.

We find no significant relationship between rock type and slope angle (Figure 17). In metamorphic, intrusive, sedimentary, and mafic volcanic rocks, landslides are typically distributed on slopes between 30° and 45°. In calcareous rocks, landslides are found on slopes from approximately 28° to 45°. The few landslides in felsic volcanic rocks occur on slopes around 40°. Overall, slopes are less steep in sedimentary and calcareous rocks compared to other rock types.

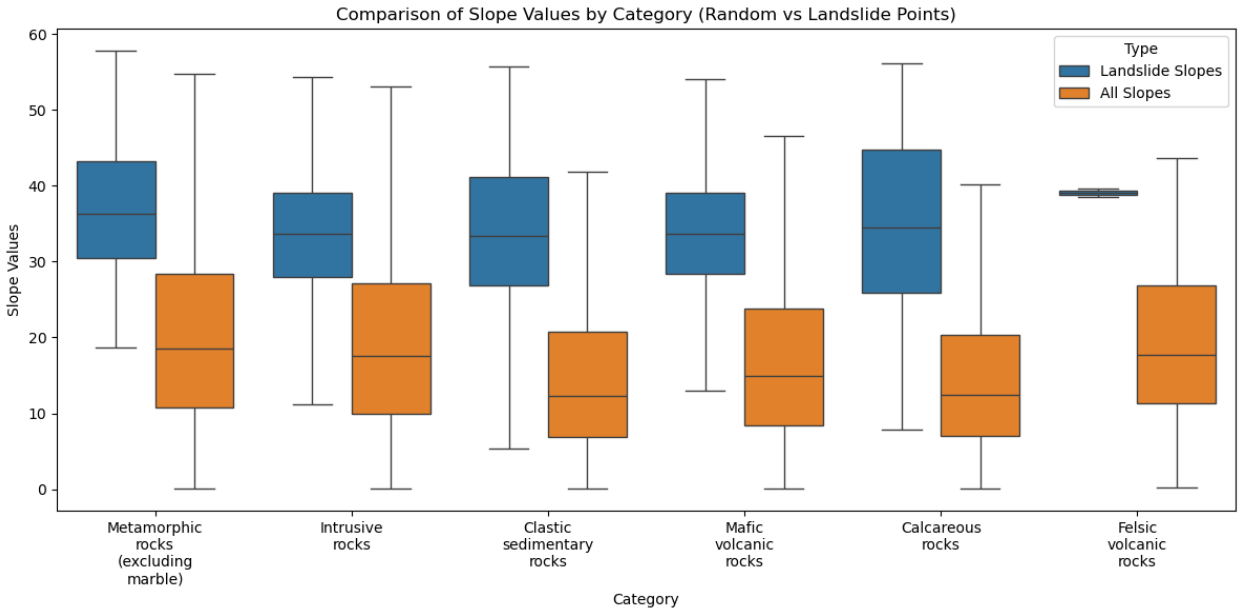

Figure 17: Distribution of landslide and study area slope values by geologic units.

Discussion

Influences on annual and seasonal trends

Our inventory shows that landslides in the study area happen most frequently from August to November while peak precipitation from the Klawock Airport weather station occurs from September to November (Figure 5). From 1980 to 2019 and across six SEAK communities, atmospheric rivers (ARs) were most frequent in August, September, October (Nash, 2024). While two of the six communities are located on PoW, all the communities span over 4 degrees of latitude and 7 degrees of longitude. Since the data from Nash (2024) represents an average across six distant communities, the specific patterns of our two communities of interest may be obscured.

The annual trends, most prominently, the 150+ landslides that occurred in 2020, require further exploration into triggering precipitation levels. Based off our observations, many of the landslides in 2020 occurred in late October, and especially damaging landslides were reported by local news sources (Stone, 2020). Our inventory can expand on the handful of landslides that ran onto roads and include landslides that occurred in more remote portions of the study area but were still triggered by the same storms. Between these spatially distant but temporally related landslides, questions about how triggering precipitation levels affect topographically different slopes can be addressed.

Barriers to precise landslide timing

This study was motivated by the advertised frequent return times of Planet Labs satellites and the spatial quality of images. Our investigation revealed that the frequency cloudy conditions expressed in the images was a barrier for determining the most precise timing for many

landslides in the study area. Additionally, from 2009 until 2016 the five PlanetScope satellites did not provide frequent imagery to constrain the timing of landsliding (Figure 6). Fortunately, the frequency of Planet imagery is only increasing such that these methods can be replicated in the future to produce a high-accuracy landslide inventory. In particular, the launch of 15 SkySat satellites promises 50 cm resolution imagery with the ability to revisit any location on Earth up to 10x daily (Planet, 2024).

Controls on landslide mobility

The forces that initiate and sustain the movement of landslides depend on the characteristics of the material itself, and the surface it is traveling on. The landslides in this inventory that develop on steep slopes (> 45°) have a relatively high average mobility value (0.5), which indicates that the runout areas were confined to areas of steep topography and therefore did not have ability to flow long distances (Figure 8). For landslides that were on shallower slopes (< 25°), the mobility values were smaller (0.3), and the runouts were longer, indicating that there less topographical confinement present. If landslides on steep slopes with high mobility values occur on coastal hillslopes and run out into water, the runout length can only be measured up to the waterline, even if material is deposited into the water body. As a result, these slides have a limited opportunity for runout. Additionally, steep slopes may have abrupt changes in slope or relief, resembling a "staircase" landscape, which can slow the movement of slide material. The relationship between mobility and slope may also depend on the volume of the landslides, which warrants further investigation. It is also possible that shallower, smaller-volume landslides are more likely to occur on steep slopes. The mobility behavior indicates that the extreme topography in SEAK and the many landslides present on coastal facing slopes, controls landslide mobility.

Explanation of relationship of density of landslides in relation to elevation

We determined that lithological unit does not appear to exert an extreme identifiable control on landslide occurrence in the study area (Figure 15-17). Rather, slope strength as a function of weathering may play an important role in soil and variably weathered and fractured bedrock (Gallen et al., 2015). Lower elevation slopes may be weaker because of being more weathered than their higher elevation counterparts, because they are both wetter and more vegetated (Gallen et al., 2017; West et al., 2002). Additionally, at lower elevations the geology is often clastic sedimentary rocks including glacial till and unconsolidated deposits which are characterized as weak (Figure 16). Therefore, we determine that landslides happen more frequently on lower elevation slopes. More precisely, 80 percent of slides happen on slopes that are less than 350 m high. In the future, we can explore the differences in precipitation amounts and intensity at various elevations with a combination of installing additional rain gauges and using modeled precipitation data that considers orographic differences (Nash, 2024). A handful of piezometers, an instrument that measures pore pressure and is useful for determining soil saturation levels, were installed across the island in June 2024, but so far, no campaigns for installing rain gauges have occurred.

Relationship between directionality of atmospheric rivers and aspect of landslides

We observe the preferential aspect of landslide occurrence and the direction of ARs, are both southerly (Figure 5 and Figure 18). If intense precipitation is preferentially falling on southern slopes because the direction of storm is from that direction, then those slopes are likely to become preferentially saturated and fail more often. Slopes that receive precipitation reach saturation more quickly and cause higher pore water pressure to develop within the soil and thus lead to landslide failure. To fully understand this, further observations and data would need to be

collected about the soil infiltration capacity, which is controlled by many factors such as the type of soil and its permeability (Cellek, 2021). While studies in Greece found that slopes facing northeast and northwest received heavy rainfall and experienced the greatest number of landslides, the relationship between the directionality of ARs and landslide aspect has not been reported before (Alexakis et al., 2014; Kouli et al., 2014).

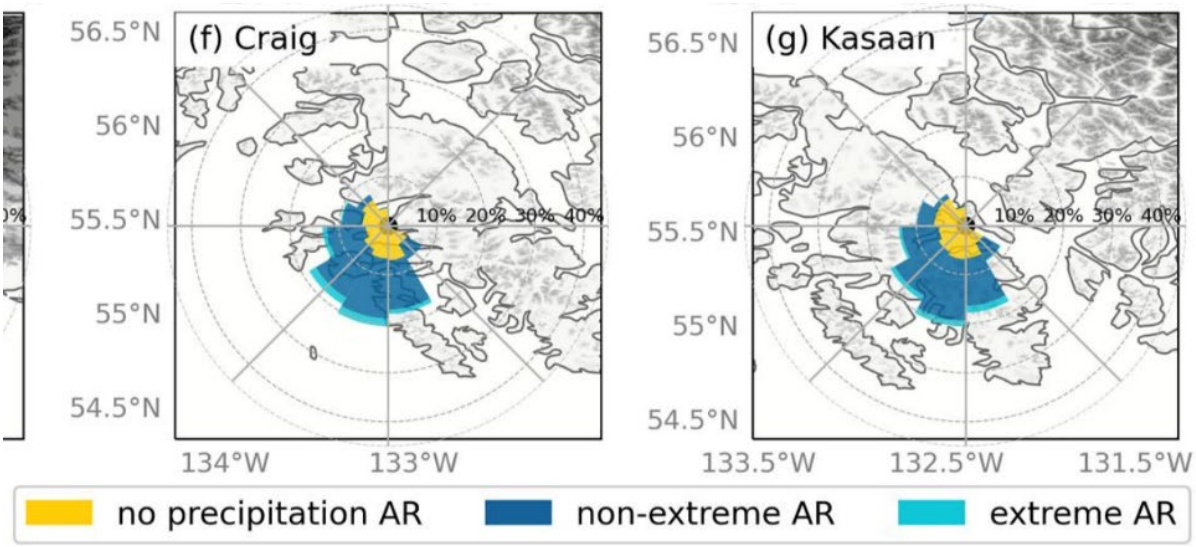

Figure 18: Wind rose diagrams for direction of atmospheric rivers (ARs) for all days when present in Craig (f) and Kasaan (g) on Prince of Wales Island, Alaska between 1 January 1980 and 31 December 2019.

The total length of each bar indicates the frequency (%) of events with vapor transport (precipitation) in that direction. The length of colored areas within the bar indicates the frequency (%) of events with precipitation <2.5 mm day^{-1} (yellow), <95th percentile precipitation (blue), and > 95th percentile precipitation (aqua) that also occurred in that direction. (Nash, 2024)

Explanation of clearcutting in the study area and relation to landslide timing

Despite local stories of recent logging operations in the study area, our early observations between landslide occurrence after clearcutting indicate a time lag of over 20 years. Our analysis of the relationship between landslide density and forest stand age relies on a GIS layer that documents the year that certain forests were clearcut. We see that across the study area, the

largest area of clearcutting occurred between 1960 and 2000, with very little harvesting done within the past approximately 25 years (Figure 19). In particular, the steep drop off indicates the underlying relevance of the Roadless Rule, a federal policy enacted in 2001 that protects national forest systems, including the Tongass National Forest, from further road construction and logging.

Since its enaction, the Roadless Rule has prohibited logging on land owned by the USFS and has caused land to be swapped and sold between the federal government and Alaska Tribal Corporations (ANCs). Alaska Native Corporations (ANCs) are private, for-profit corporations that were established by the Alaska Native Claims Settlement Act (ANCSA) of 1971 to distribute land and economic benefits to Alaska Natives (Resneck et al., 2022).

While the USFS can no longer log the forest land, the tribal corporations can and have been. From 2015 to 2020, the lower half of the Southeast Alaska panhandle saw 89 km^2 logged, 46 percent of which occurred on parcels recently transferred out of federal ownership (Resneck et al., 2022). Since the USFS had not been the primary participant of harvest operations since 2001, the data layer used to determine the timing of landslides after clearcutting gives an incomplete picture of this relationship.

Since the landslide inventory presented starts in 2009, if we were to observe a pattern of landsliding occurring one to five years after clearcutting as recorded elsewhere (Schmidt, 2001), there would have to be records of harvesting happen in 2005 at the latest. Additionally, clearcutting would need to be happening on landslide-prone slopes, in relation to slopes, elevations, and aspects. places where we are seeing landslides happen most commonly, with both slopes, elevations, and aspects. With a study area that covers such a large area, much of which

has not been harvested, statistically speaking, clearcutting may still be happening on flatter and easy to access slopes.

Since the Roadless Rule was enacted and lands have been transferred to private owners, there has been an increased interest in monitoring forest degradation in the region. Once the land is removed from the purview of Forest Service management and the strong protections for streams and waterways, it allows more aggressive harvesting practices to occur, which arguably leads to less sustainable practices. Organizations like Global Forest Watch have published datasets that track tree cover loss in the region and may better explain the relationship between clearcutting and landslide timing. Future analysis of this dataset will be undertaken.

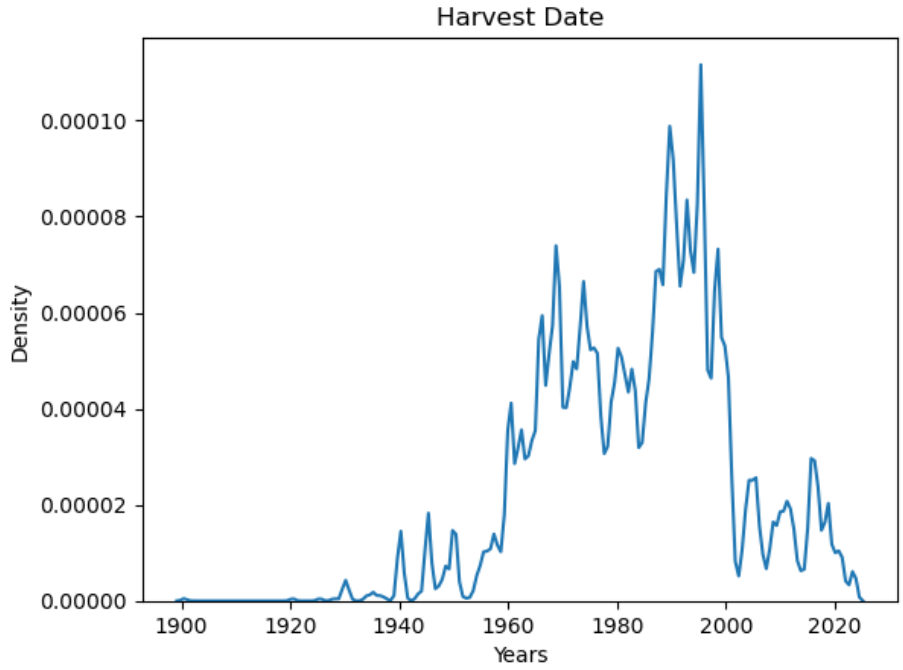

Figure 19: Distribution of the date of tree harvesting across the study area.

Conclusion

The landslide inventory presented in this study for PoW and the surrounding islands includes 766 polygon features with corresponding initiation points. The density of landslides (defined by number of landslides per unit area), showed no strong preference for lithologic units, with the densest landsliding observed at elevations of 200 m and on slopes between 30 and 40 degrees. The distribution of landslides across PoW over the past decade demonstrates a strong seasonality, with most landslides occurring between August and December. This seasonality relationship is not explained by cumulative precipitation alone but depends on the intensity and duration of storms brought on by atmospheric rivers (AR's). Additionally, we find a strong relationship between landslide location and aspect, with landslides predominantly occurring on southern slopes, which is the origin direction of AR's. Our methods also capture small landslides, revealing that most are located within 10 km of the nearest road. While earlier reports (Johnston, 2001) show that landslides on PoW happen only one to five years after clearcutting, our results indicate that the lag time is longer, with a density of landslides occurring 20 to 30 years after clearcutting. Further exploration of this relationship, including gaining additional information about privately owned and logged land, could substantiate this observed pattern.

The data presented here, especially the landslides with well-characterized timing, will provide insights into the precipitation intensity thresholds for landslide triggering. By determining the temporal and spatial distribution of landslide occurrences in the study area, we can provide valuable information to support the development of landslide early-warning systems to help inform community members about hazard levels.

Bibliography

Alaska Southeast Regional Timber Industry Task Force. 1997. *Southeast Timber Task Force Report: Prepared for Governor Tony Knowles*. Task Force. https://books.google.com/books?id=-ANJAAAAYAAJ.

Alexakis, D. D., A. Agapiou, M. Tzouvaras, K. Themistocleous, K. Neocleous, S. Michaelides, and D. G. Hadjimitsis. 2014. "Integrated Use of GIS and Remote Sensing for Monitoring Landslides in Transportation Pavements: The Case Study of Paphos Area in Cyprus." *Natural Hazards* 72 (1): 119–41. https://doi.org/10.1007/s11069-013-0770-3.

Amatya, Pukar, Dalia Kirschbaum, and Thomas Stanley. 2022. "Rainfall-induced Landslide Inventories for Lower Mekong Based on Planet Imagery and a Semi-automatic Mapping Method." *Geoscience Data Journal* 9 (2): 315–27. https://doi.org/10.1002/gdj3.145.

Amatya, Pukar, Dalia Kirschbaum, Thomas Stanley, and Hakan Tanyas. 2021. "Landslide Mapping Using Object-Based Image Analysis and Open Source Tools." *Engineering Geology* 282 (March):106000. https://doi.org/10.1016/j.enggeo.2021.106000.

Baum, Rex L., and Jonathan W. Godt. 2010. "Early Warning of Rainfall-Induced Shallow Landslides and Debris Flows in the USA." *Landslides* 7 (3): 259–72. https://doi.org/10.1007/s10346-009-0177-0.

Baum, Rex L., William H. Schulz, Dianne L. Brien, William J. Burns, Mark E. Reid, and Jonathan W. Godt. 2014. "Plenary: Progress in Regional Landslide Hazard Assessment—Examples from the USA." In *Landslide Science for a Safer Geoenvironment*, edited by Kyoji Sassa, Paolo Canuti, and Yueping Yin, 21–36. Cham: Springer International Publishing. https://doi.org/10.1007/978-3-319-04999-1_2.

Bierman, Paul, and David Montgomery. "Hillslopes." In *Key Concepts in Geomorphology,* 145-177. London: Macmillan International Higher Education, 2013.

Burns, William J, and Katherine A Mickelson. "Protocol for Deep Landslide Susceptibility Mapping," n.d.

Burns, William J, and Ian P Madin. "Protocol for Inventory Mapping of Landslide Deposits from Light Detection and Ranging (Lidar) Imagery," n.d.

Capitani, Marco, Adriano Ribolini, and Monica Bini. 2013. "The Slope Aspect: A Predisposing Factor for Landsliding?" *Comptes Rendus. Géoscience* 345 (11–12): 427–38. https://doi.org/10.1016/j.crte.2013.11.002.

Casagli, Nicola, Emanuele Intrieri, Veronica Tofani, Giovanni Gigli, and Federico Raspini. 2023. "Landslide Detection, Monitoring and Prediction with Remote-Sensing Techniques." *Nature Reviews Earth & Environment* 4 (1): 51–64. https://doi.org/10.1038/s43017-022-00373-x.

Cellek, Seda. "The effect of aspect on landslide and its relationship with other parameters." In *Landslides*. IntechOpen, 2021.

Darrow, Margaret M., Victoria A. Nelson, Michael Grilliot, Joseph Wartman, Aaron Jacobs, James F. Baichtal, and Cindy Buxton. 2022. "Geomorphology and Initiation Mechanisms of the 2020 Haines, Alaska Landslide." *Landslides* 19 (9): 2177–88. https://doi.org/10.1007/s10346-022-01899-3.

Destro, Elisa, Francesco Marra, Efthymios I. Nikolopoulos, Davide Zoccatelli, Jean Dominique Creutin, and Marco Borga. 2017. "Spatial Estimation of Debris Flows-Triggering Rainfall and Its Dependence on Rainfall Return Period." *Geomorphology* 278 (February):269–79. https://doi.org/10.1016/j.geomorph.2016.11.019.

Elliott, Julie, and Jeffrey T. Freymueller. 2020. "A Block Model of Present-Day Kinematics of Alaska and Western Canada." *Journal of Geophysical Research: Solid Earth* 125 (7): e2019JB018378. https://doi.org/10.1029/2019JB018378.

Emberson, Robert, Dalia B. Kirschbaum, Pukar Amatya, Hakan Tanyas, and Odin Marc. 2022. "Insights from the Topographic Characteristics of a Large Global Catalog of Rainfall-Induced Landslide Event Inventories." *Natural Hazards and Earth System Sciences* 22 (3): 1129–49. https://doi.org/10.5194/nhess-22-1129-2022.

Faha, Patrick. 2017. "A Comparison of Landslide Inventories Produced by Manual and Automated Methods on Timberlands in the Pacific Northwest," June. http://hdl.handle.net/1773/44992.

Guzzetti, Fausto, Francesca Ardizzone, Mauro Cardinali, Mauro Rossi, and Daniela Valigi. 2009. "Landslide Volumes and Landslide Mobilization Rates in Umbria, Central Italy." *Earth and Planetary Science Letters* 279 (3): 222–29. https://doi.org/10.1016/j.epsl.2009.01.005.

Guzzetti, Fausto, Alessandro Cesare Mondini, Mauro Cardinali, Federica Fiorucci, Michele Santangelo, and Kang-Tsung Chang. 2012. "Landslide Inventory Maps: New Tools for an Old Problem." *Earth-Science Reviews* 112 (1): 42–66. https://doi.org/10.1016/j.earscirev.2012.02.001.

Johnson, A. C., D. N. Swanston, and K. E. McGee. 2000. "LANDSLIDE INITIATION, RUNOUT, AND DEPOSITION WITHIN CLEARCUTS AND OLD-GROWTH FORESTS OF ALASKA[1]." *JAWRA Journal of the American Water Resources Association* 36 (1): 17–30. https://doi.org/10.1111/j.1752-1688.2000.tb04245.x.

Kargel, J. S., G. J. Leonard, D. H. Shugar, U. K. Haritashya, A. Bevington, E. J. Fielding, K. Fujita, et al. 2016. "Geomorphic and Geologic Controls of Geohazards Induced by Nepal's 2015 Gorkha Earthquake." *Science* 351 (6269): aac8353. https://doi.org/10.1126/science.aac8353.

Kouli, M., C. Loupasakis, P. Soupios, D. Rozos, and F. Vallianatos. 2014. "Landslide Susceptibility Mapping by Comparing the WLC and WofE Multi-Criteria Methods in the West Crete Island, Greece." *Environmental Earth Sciences* 72 (12): 5197–5219. https://doi.org/10.1007/s12665-014-3389-0.

Larsen, Isaac J., David R. Montgomery, and Oliver Korup. 2010. "Landslide Erosion Controlled by Hillslope Material." *Nature Geoscience* 3 (4): 247–51. https://doi.org/10.1038/ngeo776.

Milledge, David Graham, Dino G. Bellugi, Jack Watt, and Alexander Logan Densmore. 2021. "Automated Landslide Detection Outperforms Manual Mapping for Several Recent Large Earthquakes." Landslides and Debris Flows Hazards. https://doi.org/10.5194/nhess-2021-168.

Mtibaa, Slim, and Haruka Tsunetaka. 2023. "Revealing the Relation between Spatial Patterns of Rainfall Return Levels and Landslide Density." *Earth Surface Dynamics* 11 (3): 461–74. https://doi.org/10.5194/esurf-11-461-2023.

Nash, Deanna, Jonathan J. Rutz, and Aaron Jacobs. 2024. "Atmospheric Rivers in Southeast Alaska: Meteorological Conditions Associated With Extreme Precipitation." *Journal of Geophysical Research: Atmospheres* 129 (4): e2023JD039294. https://doi.org/10.1029/2023JD039294.

Nichol, J., and M. S. Wong. 2005. "Satellite Remote Sensing for Detailed Landslide Inventories Using Change Detection and Image Fusion." *International Journal of Remote Sensing* 26 (9): 1913–26. https://doi.org/10.1080/01431160512331314047.

Nicolazzo, J.A., K.M. Wikstrom Jones, J.B. Salisbury, and K.C. Horen. 2024. "Post-Landslide Elevation Changes Detected from Multi-Temporal Lidar Surveys of the November 2023 Wrangell, Alaska, Landslides." PIR 2024-2. Alaska Division of Geological & Geophysical Surveys. https://doi.org/10.14509/31124.

Niyokwiringirwa, Priscilla, Luigi Lombardo, Olivier Dewitte, Axel A. J. Deijns, Nan Wang, Cees J. Van Westen, and Hakan Tanyas. 2024. "Event-Based Rainfall-Induced Landslide Inventories and Rainfall Thresholds for Malawi." *Landslides* 21 (6): 1403–24. https://doi.org/10.1007/s10346-023-02203-7.

Osako, L. S. 2021. "UPDATING LANDSLIDE INVENTORY MAPS USING HIGH RESOLUTION DIGITAL ORTHOPHOTOS AND DIGITAL SURFACE AND ELEVATION MODELING: THE CASE STUDY OF BRUSQUE CITY, SANTA CATARINA STATE, BRAZIL." *ISPRS Annals of the Photogrammetry, Remote Sensing and Spatial Information Sciences* V-3–2021 (June):251–55. https://doi.org/10.5194/isprs-annals-V-3-2021-251-2021.

Patton, Annette I., Lisa V. Luna, Joshua J. Roering, Aaron Jacobs, Oliver Korup, and Benjamin B. Mirus. 2023. "Landslide Initiation Thresholds in Data-Sparse Regions: Application to Landslide Early Warning Criteria in Sitka, Alaska, USA." *Natural Hazards and Earth System Sciences* 23 (10): 3261–84. https://doi.org/10.5194/nhess-23-3261-2023.

Patton, Annette I., Joshua J. Roering, and Elijah Orland. 2022. “Debris Flow Initiation in Postglacial Terrain: Insights from Shallow Landslide Initiation Models and Geomorphic Mapping in Southeast Alaska.” *Earth Surface Processes and Landforms* 47 (6): 1583–98. https://doi.org/10.1002/esp.5336.

Prancevic, Jeff P., Michael P. Lamb, Brian W. McArdell, Christian Rickli, and James W. Kirchner. 2020. “Decreasing Landslide Erosion on Steeper Slopes in Soil-Mantled Landscapes.” *Geophysical Research Letters* 47 (10): e2020GL087505. https://doi.org/10.1029/2020GL087505.

Resneck, Jacob, Eric Stone, Edard Boyda, and Clayton Aldern. 2022. “Road to Ruin.” *Grist*. https://grist.org/project/accountability/tongass-national-forest-roadless-rule-loophole/.

Roback, Kevin, Marin K. Clark, A. Joshua West, Dimitrios Zekkos, Gen Li, Sean F. Gallen, Deepak Chamlagain, and Jonathan W. Godt. 2018. “The Size, Distribution, and Mobility of Landslides Caused by the 2015 Mw7.8 Gorkha Earthquake, Nepal.” *Geomorphology* 301 (January):121–38. https://doi.org/10.1016/j.geomorph.2017.01.030.

Schmidt, K M, J J Roering, J D Stock, W E Dietrich, D R Montgomery, and T Schaub. 2001. “The Variability of Root Cohesion as an Influence on Shallow Landslide Susceptibility in the Oregon Coast Range.” *Canadian Geotechnical Journal* 38 (5): 995–1024. https://doi.org/10.1139/t01-031.

Shao, Chongjian, Yong Li, Hengxing Lan, Pengyu Li, Rongjun Zhou, Hairong Ding, Zhaokun Yan, Shunli Dong, Liang Yan, and Tao Deng. 2019. “The Role of Active Faults and Sliding Mechanism Analysis of the 2017 Maoxian Postseismic Landslide in Sichuan, China.” *Bulletin of Engineering Geology and the Environment* 78 (8): 5635–51. https://doi.org/10.1007/s10064-019-01480-8.

Sharma, A. R., and S. J. Déry. 2020. “Contribution of Atmospheric Rivers to Annual, Seasonal, and Extreme Precipitation Across British Columbia and Southeastern Alaska.” *Journal of Geophysical Research: Atmospheres* 125 (9): e2019JD031823. https://doi.org/10.1029/2019JD031823.

Swanston, D. N. 1969. “A Late-Pleistocene Glacial Sequence from Prince of Wales Island, Alaska.” *Arctic* 22 (1): 25–33.

Swanston, Douglas N. 1970. *Mechanics of Debris Avalanching in Shallow till Soils of Southeast Alaska /*. Juneau, Alaska : Pacific Northwest Forest and Range Experiment Station, Institute of Northern Forestry, Forest Service, U.S. Dept. of Agriculture,. https://doi.org/10.5962/bhl.title.87969.

Tavakkoli Piralilou, Sepideh, Hejar Shahabi, Ben Jarihani, Omid Ghorbanzadeh, Thomas Blaschke, Khalil Gholamnia, Sansar Meena, and Jagannath Aryal. 2019. “Landslide Detection Using Multi-Scale Image Segmentation and Different Machine Learning Models in the Higher Himalayas.” *Remote Sensing* 11 (21): 2575. https://doi.org/10.3390/rs11212575.

Shao, C., Li, Y., Lan, H. *et al.* The role of active faults and sliding mechanism analysis of the 2017 Maoxian postseismic landslide in Sichuan, China. *Bull Eng Geol Environ* **78**, 5635–5651 (2019). https://doi.org/10.1007/s10064-019-01480-8.

Turner, Ted R., Steven D. Duke, Brian R. Fransen, Maryanne L. Reiter, Andrew J. Kroll, Jim W. Ward, Janette L. Bach, Tiffany E. Justice, and Robert E. Bilby. 2010. "Landslide Densities Associated with Rainfall, Stand Age, and Topography on Forested Landscapes, Southwestern Washington, USA." *Forest Ecology and Management* 259 (12): 2233–47. https://doi.org/10.1016/j.foreco.2010.01.051.

Van Westen, Cees J., Enrique Castellanos, and Sekhar L. Kuriakose. 2008. "Spatial Data for Landslide Susceptibility, Hazard, and Vulnerability Assessment: An Overview." *Engineering Geology* 102 (3–4): 112–31. https://doi.org/10.1016/j.enggeo.2008.03.010.

Wu, Tien H., William P. McKinnell Iii, and Douglas N. Swanston. 1979. "Strength of Tree Roots and Landslides on Prince of Wales Island, Alaska." *Canadian Geotechnical Journal* 16 (1): 19–33. https://doi.org/10.1139/t79-003.